Global Precipitation Extremes Associated with Diurnally Varying Low-Level Jets

Andrew J. Monaghan, Daran L. Rife, James O. Pinto, and Christopher A. Davis

National Center for Atmospheric Research,* Boulder, Colorado

John R. Hannan

Defense Threat Reduction Agency, Fort Belvoir, Virginia

ABSTRACT

Extreme rainfall events have important societal impacts: for example, by causing flooding, replenishing reservoirs, and affecting agricultural yields. Previous literature has documented linkages between rainfall extremes and nocturnal low-level jets (NLLJs) over the Great Plains of North America and the La Plata River basin of South America. In this study, the authors utilize a 21-yr, hourly global 40-km reanalysis based on the fifth-generation Pennsylvania State University–NCAR Mesoscale Model (MM5) to examine whether NLLJ–rainfall linkages are common elsewhere on the earth. The reanalysis is uniquely suited for the task because of its comparatively high spatial and temporal resolution and because a companion paper demonstrated that it realistically simulates the vertical, horizontal, and diurnal structure of the winds in well-known NLLJ regions. The companion paper employed the reanalysis to identify and describe numerous NLLJs across the planet, including several previously unknown NLLJs.

The authors demonstrate here that the reanalysis reasonably simulates the diurnal cycle, extremes, and spatial structure of rainfall globally compared to satellite-based precipitation datasets and therefore that it is suitable for examining NLLJ–rainfall linkages. A statistical approach is then introduced to categorize nocturnal precipitation extremes as a function of the NLLJ magnitude, wind direction, and wind frequency for January and July. Statistically significant relationships between NLLJs and nocturnal precipitation extremes exist in at least 10 widely disparate regions around the world, some of which are well known and others that have been undocumented until now. The regions include the U.S. Great Plains, Tibet, northwest China, India, Southeast Asia, southeast China, Argentina, Namibia, Botswana, and Ethiopia. Recent studies have recorded widespread changes in the amplitudes of near-surface diurnal heating cycles that in turn play key roles in driving NLLJs. It will thus be important for future work to address how rainfall extremes may be impacted if trends in diurnal cycles cause the position, magnitude, and frequency of NLLJs to change.

1. Introduction

a. Background

Diurnally varying low-level jets (LLJs) occur in many regions across the planet (Stensrud 1996). However, examining the causality, frequency, and impacts of these phenomena with a comprehensive and global approach has not been possible until now because of the coarse spatial (>100 km) and temporal (6-hourly) resolution of existing global reanalyses. The companion paper to this study (Rife et al. 2010, hereafter R10) introduced a new hourly, 40-km global reanalysis for 1985–2005 generated with a climate downscaling system based on the fifth-generation Pennsylvania State University–National Center for Atmospheric Research (NCAR) Mesoscale Model (MM5), termed the Climate Four Dimensional Data Assimilation System (CFDDA). CFDDA is uniquely suited for studying mesoscale features linked to the diurnal cycle across the planet, to our knowledge the first interdecadal global reanalysis with such high spatial and temporal resolution for the entire suite of three-dimensional fields. R10 employed CFDDA to examine the global distribution and characteristics of nocturnal LLJs (NLLJs). By devising an NLLJ index that minimizes

the influence of synoptic activity, R10 documented 18 regions around the globe for which NLLJs are prominent, seasonally recurring features in each hemisphere. The index resolved the known and suspected NLLJs (see Stensrud 1996) and also several previously unidentified NLLJs.

In this paper, we expand on the groundwork of R10 to examine the extent to which NLLJs around the globe are linked to nocturnal rainfall extremes. Our focus is on January and July, two months at the peak of the warm season in each hemisphere. One motivation for this work is to set a baseline for improved representation of extreme rainfall events in regions where NLLJs are not well documented but for which they may contribute to heavy rainfall that impacts adjacent populations. Many general circulation models have difficulty representing nocturnal rainfall maxima (e.g., Lee et al. 2007), a problem that may be partly due to coarse topography and a limited representation of the diurnal cycle of turbulent mixing that leads to NLLJs. An additional motivation is that climate change is altering the diurnal heating cycles that modulate NLLJs (e.g., Solomon et al. 2007), with potential impacts on the variability of nocturnal rainfall extremes in NLLJ exit regions that are associated with precipitation (e.g., Tuttle and Davis 2006). For example, it is possible that observed increases of intense precipitation episodes on the U.S. Great Plains and northwestern Midwest (Pryor et al. 2009) may be associated with a shift in the Great Plains low-level jet (GPLLJ).

b. Previous studies

Numerous studies have examined the linkage between LLJs, moisture transport, and rainfall. The majority have focused on the GPLLJ because of the relatively dense observational network available and because it has important, diurnally variable impacts on the hydrologic cycle of the United States (Wallace 1975). For example, Helfand and Schubert (1995) found that the GPLLJ contributes about 20% of the total moisture that enters the conterminous United States during the spring, with more precipitation falling at night than during the day. The nocturnal maximum of rainfall over the Great Plains has been attributed to a number of processes that affect the evolution and three-dimensional structure of the NLLJ and extreme precipitation events.

Local- and regional-scale mechanisms contribute to the relationship between the GPLLJ and rainfall on diurnal time scales. Means (1952) noted that "warm tongues" associated with jets at 850 hPa transport moisture to the northern Great Plains and are coincident with thunderstorm activity there. Pitchford and London (1962) and Hering and Borden (1962) documented linkages between summertime nocturnal thunderstorms on the northern and central Great Plains and convergence zones associated with the GPLLJ. Augustine and Caracena (1994) found that the supergeostrophic nature of the nocturnal GPLLJ enhances frontogenesis and promotes convective activity along a preexisting lower-tropospheric frontal zone near the exit region of the LLJ. Trier et al. (2006) concluded that the GPLLJ promotes a secondary circulation along the frontal zone that provides a deep layer of moist air and strong vertical wind shear to fuel long-lived nocturnal convection and enhance west–east propagation of cells. These studies establish the important role that the GPLLJ plays in transporting moisture and enhancing nocturnal rainfall in its exit region.

Large-scale mechanisms influence the GPLLJ and its coupling to rainfall on synoptic and longer time scales. Augustine and Howard (1991) noted that a strong subtropical high pressure cell centered over the southeastern United States coupled with a well-defined low pressure cell over the western United States coincided with a strengthened GPLLJ and set up an environment favorable for enhanced periods of mesoscale convective activity on the central and northern U.S. plains during summer in 1986 and 1987. Arritt et al. (1997) found that the 1993 floods on the upper Mississippi River basin were associated with a high incidence of strong LLJs, which Byerle and Paegle (2003) attributed to enhanced cross-mountain upper-level zonal flow over the Rocky Mountains in the western United States. Weaver and Nigam (2008) linked warm-season GPLLJ-modulated rainfall variability to large-scale forcing from the El Niño–Southern Oscillation (ENSO) and the North Atlantic Oscillation (NAO). Mo and Berbery (2004) found that there is an inverse relationship between the strength of the GPLLJ and the Gulf of California LLJ (GCLLJ) that is related to the upper-level jet streams. Strong GPLLJ (GCLLJ) cases coincide with weaker GCLLJ (GPLLJ) cases and less summer rainfall over the southwestern United States (central United States and Mississippi Valley). These studies demonstrate the importance of upper-level long-wave patterns in modulating the intraseasonal and interseasonal variability of the GPLLJ and consequently the positioning and persistence of associated rainfall maxima.

In addition to the U.S. Great Plains, numerous studies have linked LLJs and rainfall variability in regions around the world: for example, South America (e.g., Nogués-Paegle and Mo 1997), Africa (Zunckel et al. 1996; Zhang et al. 2006), India (Findlater 1969; Joseph and Sijikumar 2004), and the western Pacific (Chen and Yu 1988; Miller and Fritsch 1991). A growing body of literature focuses on the Southern Hemisphere counterpart of the GPLLJ, the South American LLJ (SALLJ). Vera et al. (2006)

summarized the South American Low Level Jet Experiment (SALLJEX). SALLJEX employed an enhanced network of balloon soundings and rain gauges throughout the La Plata River basin, along with a series of aircraft observational flights from November 2002 to February 2003, to examine the detailed structure of the LLJ. Vera et al. (2006) emphasized the importance of understanding the SALLJ and its hydrological–climatic impacts, because 50% of the combined populations of Brazil, Argentina, Paraguay, Uruguay, and Bolivia reside in the La Plata basin.

Nogués-Paegle and Mo (1997) found that precipitation is enhanced in southern Brazil and central Argentina because of the southward transport of tropical moisture by the SALLJ. Salio et al. (2002) established that a subset of SALLJ events, called Chaco jet events (CJEs), transport nearly an order of magnitude more low- and mid-level moisture from the Amazon southward to the central plains compared to the summer mean and account for 55% of the summer precipitation over northeastern Argentina. Nicolini and Saulo (2006) found that nocturnal rainfall maxima in the exit regions of CJEs were related to enhanced low-level convergence associated with the jets. Similarly, Salio et al. (2007) connected SALLJ variability to a nocturnal preference for the occurrence of mesoscale convective systems. Several researchers have hypothesized that the ENSO cycle modulates the SALLJ and the accompanying rainfall (Vernekar et al. 2003; Marengo et al. 2004). The SALLJ studies collectively indicate that the local- and large-scale mechanisms that drive the SALLJ and its connection to nocturnal rainfall are comparable to those for the GPLLJ. The similarity between the GPLLJ and SALLJ mechanisms that influence rainfall suggests that analogous forcing may link rainfall and NLLJs across the planet.

c. Overview of current study

Here we take advantage of the 21-yr, hourly, 40-km CFDDA reanalysis to examine the association between land-based NLLJs and rainfall extremes globally. R10 compared CFDDA to a global reanalysis and to independent observations within both the U.S. Great Plains and South America and showed that CFDDA reasonably reproduces the mean structure and diurnal cycle of winds, indicating that it is useful for the study of NLLJs. Similarly, in section 2 we compare CFDDA rainfall to two observationally based datasets and demonstrate that CFDDA resolves the mean structure, intensity, and diurnal cycle of rainfall and thus is suitable for examining how NLLJs are associated with rainfall extremes. In section 3, the methodology by which NLLJs are linked with nocturnal rainfall extremes is outlined. Results and

discussion are presented in section 4, and conclusions are drawn in section 5. The reader is referred to R10 for a complete description of the model configuration and datasets used to generate CFDDA.

2. Analysis and verification of CFDDA rainfall

The objective of this section is to verify CFDDA's representation of 1) the global spatial patterns of rainfall, 2) the global occurrences of rainfall extremes, and 3) the global diurnal cycle of rainfall. Two satellite-based precipitation datasets are used for the evaluation. The first dataset is the Climate Prediction Center Morphing Technique (CMORPH), which uses precipitation estimates from low orbiting satellite microwave observations whose features are transported by spatial propagation information from geostationary infrared satellite data (Joyce et al. 2004). The version of CMORPH used in this study is a 1-hourly, ~8-km-resolution product, making it well suited for comparison to the diurnal cycle in CFDDA. The second dataset is the Global Precipitation Climatology Project 1 Degree Daily Combination product (GPCP), which is a companion to the GPCP Version 2.1 Combination (Adler et al. 2003). GPCP synthesizes a variety of gauge data and satellite radiances, including microwave, infrared, infrared sounder, and outgoing longwave radiation. Because of its limited temporal resolution (daily), the GPCP data are only used for comparison with the long-term global median precipitation values in CFDDA. For consistency, both CMORPH and GPCP are remapped to the nominal 40-km grid of CFDDA using the conservative remapping algorithm available in the Spherical Coordinate Remapping and Interpolation Package (SCRIP; Jones 1999). The following figures span 3 yr that overlap both CMORPH and CFDDA, 2003–05.

Figure 1 shows the 3-yr median daily rainfall in CMORPH, GPCP, and CFDDA for January and July. CFDDA tends to produce higher median rainfall over most regions compared to CMOPRH and GPCP, but not outside of the bounds of uncertainty among the various estimates (e.g., Ebert et al. 2007). All three datasets have similar patterns of rainfall during both seasons. To quantify the similarity, Spearman rank pattern correlations (e.g., Wilks 2006; Rodgers and Nicewander 1988) were performed on the data from 60°N to 60°S across all longitudes. The correlation between GPCP and CFDDA is 0.80 in both seasons, indicating remarkably similar patterns, whereas the correlation between CMORPH and CFDDA is much lower (0.51). Visual inspection suggests that the greatest differences between CMORPH and both CFDDA and GPCP lie near the northern and southern peripheries of the maps
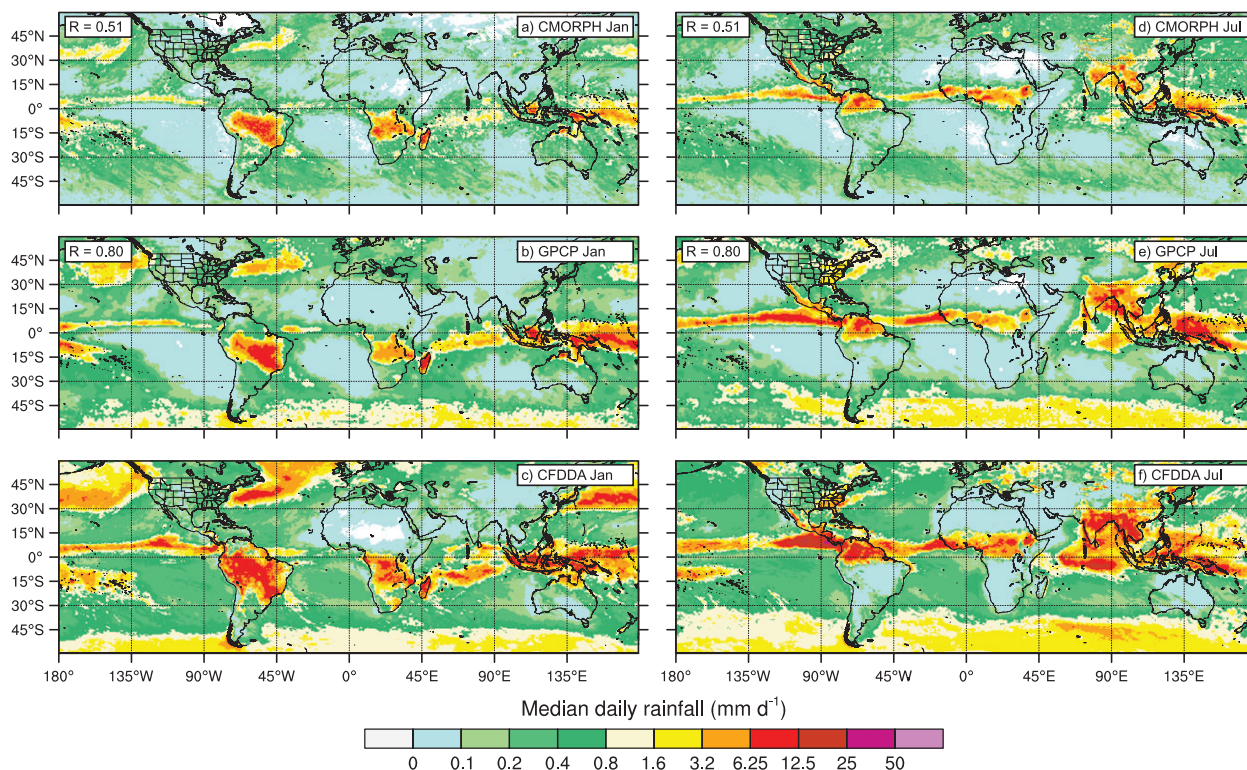
FIG. 1. The median daily rainfall (mm day^{-1}) for 2003–05 for (top) CMORPH, (middle) GPCP, and (bottom) CFDDA for (a)–(c) January and (d)–(f) July. The Spearman rank correlations between CFDDA and CMORPH and between CFDDA and GPCP are shown in the top-left corners of (a),(b),(d), and (e).

(>45° latitude). The precipitation patterns are more strongly correlated between 30°N and 30°S (~0.7), suggesting a reduced fidelity of the CMORPH estimates at higher latitudes (>45° latitude). Indeed, Joyce et al. (2004) reported that CMORPH estimates are questionable at high latitudes because of the contamination of retrievals over the snow and ice cover that is often present in these regions. In addition, Janowiak et al. (2005) noted that CMORPH produces about 33% lower precipitation over the oceans compared to GPCP, but they were unable to explain the difference.

Figure 2 shows the 90th percentile of the peak hourly rainfall occurring between 0000 and 0400 LST for 2003–05 for CMORPH and CFDDA during January and July. Each hourly output is assigned the local time within each 15° longitudinal strip on the globe; for example, the 0600 UTC output over the Great Plains region, centered at 100°W, is assigned a time of 0000 LST. Longitudinal strips for a given local time are then combined to form global maps of rainfall occurring at 0000, 0100, and 0200 LST and so forth. Finally, the 90th percentile of maximum rainfall values occurring between 0000 and 0400 LST are calculated for each day for 2003–05 ($N = 93$ days for each month). The comparison of

CMORPH and CFDDA for 0000–0400 LST provides a measure of CFDDA's ability to simulate extreme rainfall events for the hours after local midnight, when NLLJs typically have their most important impact on rainfall (e.g., Higgins et al. 1997; Nicolini and Saulo 2006). CMORPH was found to reasonably reproduce the diurnal cycle over the United States compared to hourly gauge precipitation estimates (Janowiak et al. 2005) and thus provides a reasonable estimate of nocturnal precipitation over land. Both datasets have distinct nocturnal maxima in the tropics and in the middle latitudes for the respective warm season in each hemisphere. Some of the nocturnal maxima coincide with well-known NLLJ exit regions. For example, both datasets have a maximum during austral summer (January) in South America near 35°S, near the exit region of the SALLJ. A maximum can also be distinguished in both datasets over the Great Plains during boreal summer (July), corresponding to the GPLLJ, although it is weaker in CFDDA. An analysis of the National Centers for Environmental Prediction (NCEP) stage-IV radar/gauge-based U.S. precipitation data for July 2003–05 (Lin and Mitchell 2005; not shown because it is not a global dataset) suggests that the CMORPH nocturnal rainfall maxima in the GPLLJ exit
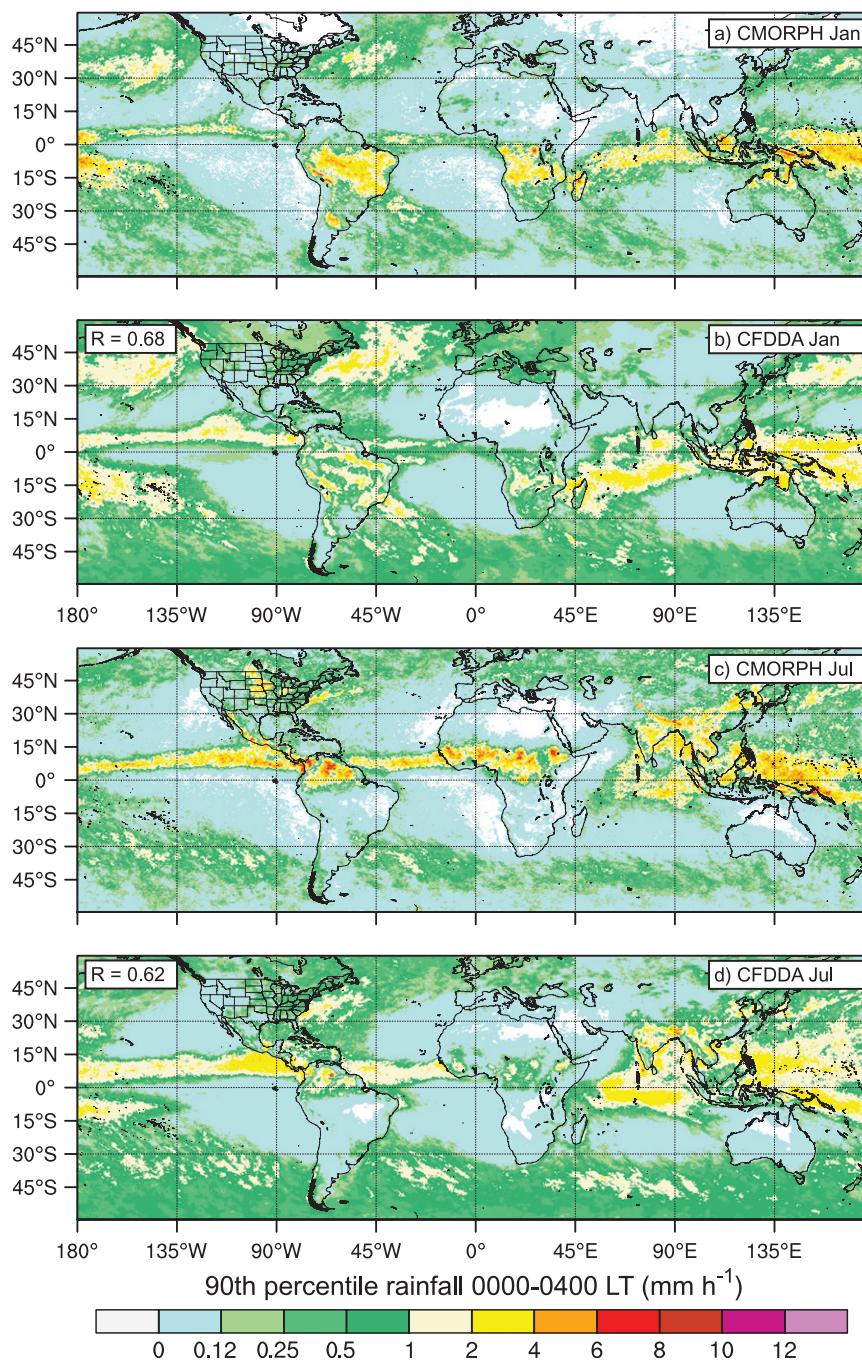
FIG. 2. The 90th percentile of the peak hourly rainfall (mm h^{-1}) occurring between 0000 and 0400 LST for 2003–05 for CMORPH and CFDDA for (a),(b) January and (c),(d) July. The Spearman rank correlations between CFDDA and CMORPH are shown in the top-left corners of (b) and (d).

region may be somewhat overestimated. The stage-IV 90th percentile rainfall values are more similar to those in CFDDA over the northern central United States, although they are still larger than those found in CFDDA near the convergence of the Nebraska, Iowa, and South Dakota borders. In general, the nocturnal maxima in CFDDA are slightly weaker compared to CMORPH at low latitudes (<30° latitude) and slightly stronger at high latitudes (>30° latitude). The Spearman rank pattern correlations between the two datasets are 0.68 (January)

and 0.62 (July), indicating relatively strong correspondence in their depictions of nocturnal maxima.

Figure 3 shows the normalized amplitude of the mean diurnal cycle of rainfall for 2003–05 for CMORPH and CFDDA for January and July. The amplitude is expressed as the difference between the frequency of rainfall at the peak and base of the diurnal cycle at each grid point, for precipitation meeting or exceeding a threshold of 0.2 mm h^{-1}, following the convention of Knievel et al. (2004). Thus, a location at which rain falls at the same time every day and for which it never rains at another time of day will have an amplitude of one. Where there is an equal frequency of rainfall at all hours, the amplitude is zero. The Spearman rank pattern correlations (0.53 in January; 0.61 in July) indicate that the spatial distribution of the diurnal cycle is generally similar between CFDDA and CMORPH, even in the presence of noise that is commonly found in precipitation estimates (Ebert et al. 2007). During austral summer (January), both datasets capture the diurnal cycle of rainfall in the Amazon basin, southern Africa, and the islands in Southeast Asia noted by others (e.g., Dai 2001). In boreal summer (July), both datasets capture the diurnal cycle over the Rocky Mountains and the southeastern United States (e.g., Knievel et al. 2004), northern South America, India, and China (Dai 2001). The amplitude of the diurnal cycle is generally larger and more widespread in CFDDA in both seasons, although it is uncertain which dataset has a more realistic depiction over most of the globe. Over the United States, the hourly stage-IV radar/gauge precipitation dataset is employed to gain additional perspective on the rainfall's diurnal cycle. A comparison with stage-IV for July 2003–05 (not shown) indicates that CMORPH, CFDDA, and stage-IV all have a similar warm-season diurnal cycles over the Great Plains, but CFDDA has a larger diurnal cycle than stage-IV and CMORPH over the southeastern United States. It is possible that the latter is due to the convective parameterization in CFDDA, which may be too easily triggered in regions with strong solar heating. The timing of the peak amplitude of the diurnal cycle was found to be comparable between CFDDA and CMORPH (not shown), although CFDDA tends to reach its diurnal maximum earlier in the day by about 2–4 h compared to CMORPH. A similar tendency was found for the Community Climate System Model, version 2 (CCSM2) by Dai and Trenberth (2004) and was attributed to the limitations of the convective parameterization. Despite the earlier peaks, CFDDA resolves the strong diurnal gradients that exist in many NLLJ areas, such as in the GPLLJ region during July (e.g., Carbone and Tuttle 2008) and the SALLJ region during January.

In summary, CFDDA generally captures the long-term median, nocturnal extremes, and diurnal cycle of rainfall compared to GPCP and CMORPH. The characteristics of rainfall in CFDDA are within the bounds of uncertainty among the various datasets available (e.g., Ebert et al. 2007), indicating that CFDDA is suitable for the subsequent analysis in which we compare the linkages between NLLJs and nocturnal rainfall extremes. In the following section, we describe the methodology with which these linkages are examined.

3. Methodology

a. Calculation of the nocturnal LLJ index

To identify NLLJs in a consistent manner globally, R10 devised an index that exploits the comparatively high temporal resolution of the global CFDDA dataset. The winds at each grid point are classified as being associated with an NLLJ according to two criteria, and both must be satisfied simultaneously. The first requires the winds at 500 m AGL (near jet level) to be stronger at local midnight than at local noon. The second requires the wind speed at the jet's core (500 m AGL) to be stronger than that aloft (4 km AGL), similar to the criterion of Whiteman et al. (1997). The NLLJ index (m s^{-1}) is therefore both a function of the difference between winds near the surface and those aloft and the diurnal variation of the winds. Given these rules, the NLLJ index $NLLJ$ is defined at each grid point according to

$$NLLJ = \lambda \varphi \sqrt{[(u_{00}^{L1} - u_{00}^{L2}) - (u_{12}^{L1} - u_{12}^{L2})]^2 + [(v_{00}^{L1} - v_{00}^{L2}) - (v_{12}^{L1} - v_{12}^{L2})]^2}, \qquad (1)$$

where u and v are the zonal and meridional wind components, respectively. The superscripts $L1$ and $L2$ denote winds at 500 and 4000 m AGL, respectively, and represent winds within the jet core and above the core. As shown in R10, the various jets are at their maximum at about 500 m AGL, consistent with the 300–600-m mean height range for the Great Plains NLLJ reported by Whiteman et al. (1997) and others. The subscripts 00 and 12 denote local midnight and local noon. Because the term under the square root is positive, two additional terms are needed to account for the algebraic signs of the vertical and temporal changes in the wind. The first, lambda λ, is a digital multiplier that requires the difference between the 500-m-AGL wind speed
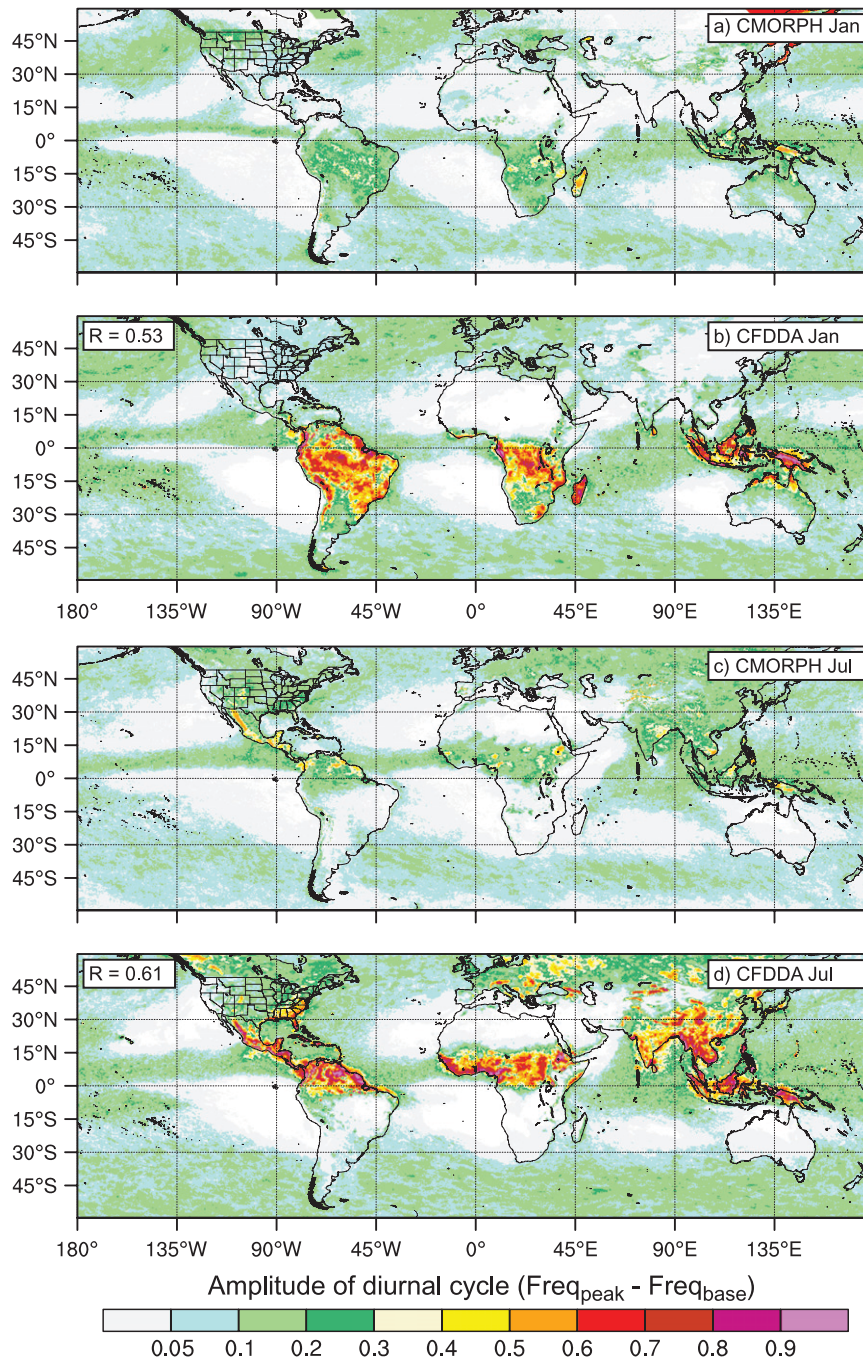
FIG. 3. Normalized amplitude of the mean diurnal cycle of precipitation for 2003–05 for CMORPH and CFDDA for (a),(b) January and (c),(d) July. The amplitude is expressed as the difference between the frequency of rainfall at the peak and base of the diurnal cycle at each grid point, for precipitation meeting or exceeding a threshold of 0.2 mm h^{-1}. The Spearman rank correlations between CFDDA and CMORPH are shown in the top-left corners of (b) and (d).

at local midnight and local noon to be positive. The second, phi φ, is also a digital multiplier that requires the 500-m-AGL wind speed at local midnight to be greater than that at 4000 m AGL at the same time. This ensures that the winds conform to a jet-like profile. The equations for λ and φ are given in R10. Experimentation with several variants of Eq. (1) demonstrated that this version is effective at filtering out
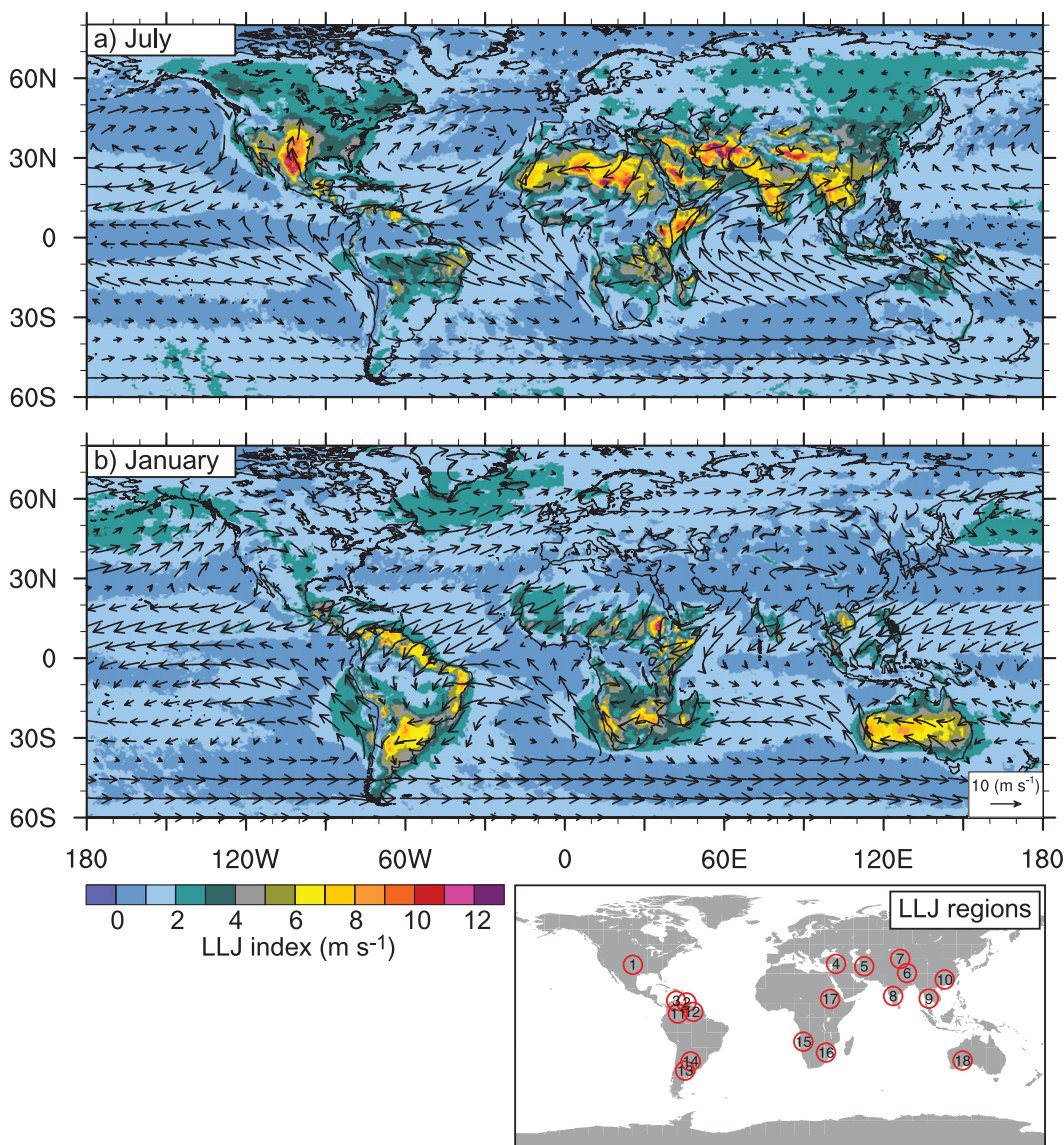
FIG. 4. Mean NLLJ index (shaded) at 0000 LST for 1985–2005 for (a) July and (b) January. The mean 500-m-AGL winds (arrows) are plotted atop the NLLJ index at approximately every 20th grid point (~10°). Numbered boxes in the inset correspond to NLLJs examined in this study, whose characteristics are summarized in Table 1.

synoptically driven winds that may otherwise appear to be NLLJs.

Figure 4 shows the 21-yr mean of the daily NLLJ index maps ($N = 651$) for January and July. The mean 0000 LST wind vectors at ~500 m AGL are also shown to provide a sense of the primary direction and geographic orientation of the NLLJs. The inset in Fig. 4 shows the regions with strong NLLJ activity analyzed for this study. Table 1 provides a brief description and summary statistics for each region. The NLLJ regions selected for analysis were chosen either because of their known or suspected link to intense precipitation events (e.g., South America,

China) or because they were not previously identified in the literature (e.g., Syria, Iran). In the interest of efficiency, we do not present statistics for every NLLJ region identified in Fig. 1. Next, a consistent and quantitative methodology is described for examining the relationship between the NLLJs and nocturnal rainfall extremes for each of the selected regions.

b. Regional NLLJ and rainfall calculations

Precipitation characteristics for each NLLJ region are computed within a visually defined box centered on the

TABLE 1. NLLJ characteristics and relationship with nocturnal rainfall extremes (see Fig. 4 for locations). The primary wind direction (fourth column) is the direction toward which the wind blows, to be consistent with the notation in Figs. 6–16. In columns 9–11, the ratio of $P_{90}^{Upper}/P_{90}^{Lower}$ is shown for each of the eight directional boxes (see Fig. 6 for locations). Further explanation is given in section 4.

No.	Region	Most active month	Primary downstream direction for upper 10th percentile of NLLJ events	Frequency of winds blowing in primary downstream direction %	Mean wind speed in primary downstream direction m s⁻¹	P_{90}^{Upper} primary box mm h⁻¹	P_{90}^{Lower} primary box mm h⁻¹	$P_{90}^{Upper}/P_{90}^{Lower}$ each directional box							
		—	—					N	NE	E	SE	S	SW	W	NW
1	GPLLJ	Jul	N	47	15	0.39	0.01	44.7[ab]	16.4[a]	0.7	0.2	0.3	0.9	2.3[a]	27.1[a]
2	North Venezuela	Jul	W	96	13	1.20	0.84	0.9	1.1	1.5[a]	1.1	1.1	1.6[a]	1.4[b]	1.3
3	Maracaibo	Jul	W	81	14	0.44	0.54	1.0[a]	1.4[a]	1.0	1.2	2.8[a]	1.0	0.8[b]	0.5
4	Syria	Jul	SE	35	13	0.00	0.00	0.3	0.7	0.0	0.0[b]	0.0	0.6	0.5	0.3
5	Iran	Jul	W	47	17	0.00	0.00	61.1[a]	0.0[a]	0.0[a]	0.0	0.0	0.0	0.4[b]	2.1[a]
6	Tibet	Jul	E	33	13	0.28	0.09	9.1[a]	5.2[a]	3.0[ab]	1.0[a]	1.2[a]	0.8	1.8[a]	4.8[a]
7	Tarim Pendi	Jul	SW	38	12	0.15	0.01	1.2	0.0	0.1	0.2	3.9[a]	13.1[ab]	58.6[a]	4.8[a]
8	India	Jul	E	95	21	0.95	0.54	5.4[a]	5.7[a]	1.8[ab]	1.0	0.9	1.1[a]	1.9[a]	4.2[a]
9	Southeast Asia	Jul	NE	51	14	0.99	0.44	1.2[a]	2.3[ab]	1.4[a]	1.1[a]	1.1	1.2[a]	1.0[a]	0.8
10	China	Jul	N	43	13	0.53	0.16	3.4[ab]	1.2	0.4	0.5	0.6	0.7	1.0	2.6[a]
11	Venezuela[c]	Jan	SW	66	15	0.20	0.60	0.0	0.2	0.2	0.5	0.4	0.0[b]	0.0	0.0
12	Guyana[c]	Jan	SW	91	14	0.69	1.01	0.5	0.7[a]	0.2	0.7	0.7	0.7[b]	0.3	0.3
13	Argentina	Jan	SW	45	14	0.78	0.04	0.4	0.1	0.2	2.9	19.2[a]	11.5[ab]	1.8	0.3
14	Brazil	Jan	W	40	13	0.32	0.14	1.1	2.4[a]	0.9	0.1	0.5	2.3[a]	0.5[b]	0.5
15	Namibia	Jan	E	27	10	1.13	0.20	1.1	1.3[a]	5.7[a]	9.4[a]	5.7[a]	1.5[a]	0.7	0.4
16	Botswana	Jan	W	49	16	0.47	0.06	23.9[a]	6.8[a]	4.2[a]	3.4[a]	3.3[a]	4.2[a]	8.3[ab]	16.9[a]
17	Ethiopia[c]	Jan	S	44	12	0.04	0.01	3.7[a]	2.6[a]	2.5[a]	1.6[a]	4.0[ab]	1.5	0.0	0.0
18	Australia	Jan	W	38	15	0.20	0.20	0.7[a]	1.8[a]	0.8	0.4	0.3	0.3	0.8[a]	1.1[a]

[a] The rainfall distributions for the top vs bottom 10th percentile of NLLJ events in the given rainfall box are statistically distinct ($p < 0.001$).

[b] This box corresponds to the primary exit region (as defined by the most frequent wind direction).

[c] Season of maximum activity is during winter in LLJ's hemisphere.

NLLJ's climatographical mean core for each region (e.g., see the white boxes in Figs. 6a, 7a, 8a, 9a, 10a, 11a) for the season having the strongest NLLJ (January or July) in a given location. Box sizes depend on the horizontal scale and geographic orientation of each jet, but typically they encompass a 10°–15° latitudinal extent and a 15° longitudinal extent. A daily regional NLLJ index is defined by spatially averaging the daily NLLJ index values for all grid points within each box. The resulting index is a 21-yr time series of daily NLLJ values in each region for January and July (for each month, $N = 21$ yr $\times$ 31 days = 651). The daily regional NLLJ index values are then rank ordered and divided into 10 equal bins ($N = 65$ NLLJ events per bin).

Next, a methodology is devised to determine whether nocturnal rainfall extremes are associated with the terminus of NLLJs, as expected (e.g., Tuttle and Davis 2006). For each region, eight "rainfall boxes," each having the same dimensions as their parent LLJ core box, are constructed around the perimeter of the NLLJ region, as shown in Fig. 5. The hypothesis is that the precipitation accumulation in the boxes downstream from the jet maximum will be larger than in the upstream boxes.

Rainfall is analyzed from 0000 to 0400 LST, representative of nocturnal precipitation coincident with or immediately following the 0000 LST time at which the NLLJ index is calculated. For each of the eight rainfall boxes, the distribution of daily 0000–0400 LST mean rainfall values ("nocturnal rainfall") at every grid point is conditionally sampled based on the NLLJ's strength and divided into 10 deciles. For example, for each box the nocturnal rainfall values corresponding to the weakest ($\leq$10th percentile) NLLJ events are sorted into one bin, and those rainfall values corresponding to the strongest ($\geq$90th percentile) NLLJs are sorted into another bin. Then, for each of the eight rainfall boxes, the ratio of the 90th percentile of nocturnal rainfall from the strongest NLLJ events (P_{90}^{Upper}) to the 90th percentile rainfall from the weakest NLLJ events (P_{90}^{Lower}) is computed. The 90th percentile rainfall value is chosen because it provides a proxy of typical rainfall extremes, whereas the maximum (i.e., 100th percentile value) may represent a spuriously large rainfall value. The sample size in each rainfall box is equal to the number of grid points multiplied by the number of days in the bin. For example, a (10×10) grid point box would have (10 grid points east $\times$ 10 grid points north $\times$ 65 NLLJ events) for a total of 6500 rainfall values in a given percentile bin. The resulting ratio of $P_{90}^{\mathrm{Upper}}/P_{90}^{\mathrm{Lower}}$ provides a measure of whether the nocturnal rainfall in a given rainfall box surrounding the jet region is related to the strength of the jet. A ratio greater than 1.0 indicates that the strongest NLLJ events produce more rainfall than the weakest
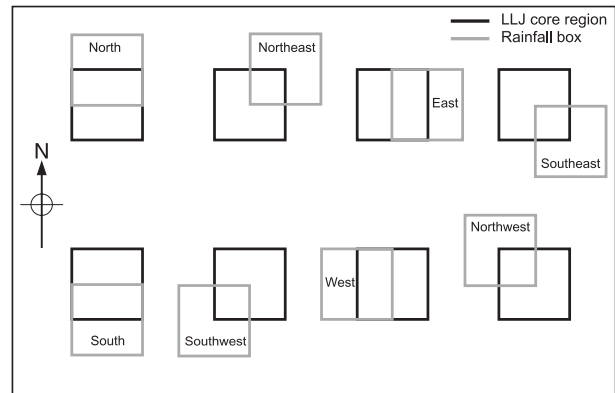

FIG. 5. Schematic of the eight-box technique used to quantify the relationship between NLLJ events and precipitation. Black boxes encompass the NLLJ core, and gray boxes, each having the same dimensions as their parent LLJ core box, are used to examine the rainfall upstream and downstream of the LLJ core.

events. The identification of a nocturnal rainfall extreme in a given rainfall box does not necessarily imply that the NLLJ causes the greater rainfall; the proximity of the rainfall box to the NLLJ exit region is also important. Therefore, the wind rose climatology is computed within the "jet core box" for the strongest ($\geq$90th percentile) NLLJ events. The dominant spike or spikes in the wind rose point toward the jet exit region. Again, the hypothesis is that the precipitation ratio in the boxes downstream from the jet maximum will be larger than the ratio in the upstream boxes. Such a result would implicate the jet[1] as the controlling factor in nocturnal rainfall. Additionally, Mann–Whitney U tests (Mann and Whitney 1947) are applied to the conditional rainfall distributions for the strongest and weakest NLLJ events in each rainfall box to determine whether the distributions are statistically distinct. In the following section, we present results from our analysis of the linkages between NLLJ and nocturnal rainfall extremes; further details on the methodology are provided as necessary.

4. Results and discussion

Here we examine the linkages between NLLJs and nocturnal rainfall extremes with particular focus on six regions. The regions are chosen because they provide

---

[1] The association between the jet exit region and precipitation must involve organized upward motion. Ascent is not necessarily associated with a jet exit region, because diffluent flow can be nondivergent. However, the terminus of the jet is usually at a front or a topographic feature. In the former case, frontogenesis often occurs; in the later, there is topographically forced upglide. Either way, ascending motion results.

a representative sample of well-known jets (U.S. Great Plains, northern Argentina) and lesser known or newly identified jets (Tarim Pendi, China, Namibia–Angola, and Syria) that may or may not impact nocturnal rainfall. Table 1 summarizes the NLLJ/rainfall characteristics for all 18 regions in the study.

The results for the GPLLJ in boreal summer are presented in Fig. 6. R10 compared CFDDA to independent observations from the National Oceanic and Atmospheric Administration (NOAA) Profiler Network and found that CFDDA accurately represents the vertical and diurnal structure of the GPLLJ. The top two panels (Figs. 6a,b) provide an overview of the terrain, the magnitude of the NLLJ index and 0000 LST surface wind vectors for the strongest ($\geq$90th percentile) events, and the location of the central NLLJ box (white) and the rainfall box for the primary NLLJ exit region (red). The jet structure and general south-southwesterly flow is consistent with numerous studies (e.g., Bonner 1968; Mitchell et al. 1995; Whiteman et al. 1997; Song et al. 2005). The distributions of wind direction and wind speed for the strongest GPLLJ events are shown in Fig. 6c (note that wind flags indicate the direction that the wind is blowing toward).

Around the perimeter of the wind rose is the ratio of the 90th percentile of precipitation for the strongest (P_{90}^{Upper}) and the weakest (P_{90}^{Lower}) GPLLJ events for each of the rainfall boxes (Fig. 5). There is a clear relationship between the GPLLJ exit region and nocturnal precipitation, with ratios exceeding 10 in the northeast, north, and northwest rainfall boxes. The rainfall distributions for the strongest and weakest GPLLJ events are statistically distinct ($p < 0.001$) for the northeast, north, northwest, and west rainfall boxes (Table 1). Figure 6d shows the distributions of precipitation for the strongest and weakest GPLLJ events within the dominant (northern) exit region of the GPLLJ, confirming the enhanced rainfall occurring with the strongest GPLLJ events. For clarity, note that the P_{90}^{Upper} (0.39 mm h^{-1}) and P_{90}^{Lower} (0.01 mm h^{-1}) values that are used to calculate the ratio for the northern box shown in Fig. 6c represent the 90th percentile rainfall value for the two distributions shown in Fig. 6d. The 90th percentile values for both distributions fall into the first bin in this example because of the strongly skewed precipitation distribution (which is why a logarithmic axis is employed). Ratios for the other boxes are calculated in the same manner. The results shown in Fig. 6 agree with previously established linkages between the GPLLJ strength and rainfall maxima in the exit region (Mo and Berbery 2004; Tuttle and Davis 2006), demonstrating that our methodology is robust for examining similar linkages in less-studied locations.

Figure 7 is shows similar results for the Argentina NLLJ in January, a region where the SALLJ is strongly manifested (Brazil is another; see Fig. 1 and Table 1). The SALLJ is also regularly observed farther equatorward, in Bolivia and Paraguay (e.g., Vera et al. 2006). We focus here on Argentina because our NLLJ index suggests that the diurnally varying component of the SALLJ is most prevalent in northern Argentina (Fig. 4b). It is worth noting that R10 compared independent pilot balloon soundings taken during the July 2003 SALLJEX field season to CFDDA for sites in northern Argentina and Brazil and found that CFDDA reasonably reproduces the diurnal cycle and structure of the SALLJ. The rainfall is strongly enhanced in the south and southwest rainfall boxes (the primary exit region) during strong NLLJ conditions (Fig. 7c). The rainfall for the strongest and weakest NLLJ events for the south and southwest rainfall boxes are statistically distinct as shown in Table 1. There are several rainfall values along the tail of the rainfall distributions for the south rainfall box (Fig. 7d) for which the rainfall frequency during the strongest NLLJ events exceeds that during the weakest NLLJ events by nearly an order of magnitude.

The results for the newly identified Tarim Pendi NLLJ in northwest China in boreal summer are presented in Fig. 8. R10 confirmed the existence of the Tarim Pendi NLLJ from soundings at Kuqa (41.7°N, 82.9°E) and noted that it forms in the arid Tarim Basin between the Tibetan Plateau to the south and the Tian Shan Mountains to the north (Fig. 8a). A case study performed by R10 suggests the Tarim Pendi NLLJ is related to cold fronts that are deflected around the Tian Shan's eastern edge, such that cold air enters the basin from the east and northeast (Fig. 8b). Nocturnal rainfall extremes are associated with the exit regions of the Tarim Pendi NLLJ (Fig. 8c). There are statistically significant differences between the rainfall distributions for the weakest and strongest Tarim Pendi NLLJ events for the south, southwest, west, and northwest rainfall boxes (Table 1). Higher-intensity rainfall (>1 mm h^{-1}) is considerably more frequent during the strongest NLLJ events in the southwest rainfall box (Fig. 8d). Our result suggests that the Tarim Pendi NLLJ makes an important contribution to warm-season moisture transport and precipitation in this otherwise arid region.

The results for the NLLJ in southwest China in boreal summer are shown in Fig. 9. The China NLLJ has been associated with nocturnal mesoscale convective activity by Miller and Fritsch (1991) and Stensrud (1996), though neither study linked them in a quantitative manner. Like the GPLLJ, the China NLLJ lies to the east of a major mountain range and transports moisture poleward from a warm-water source located to the south (Fig. 9b versus
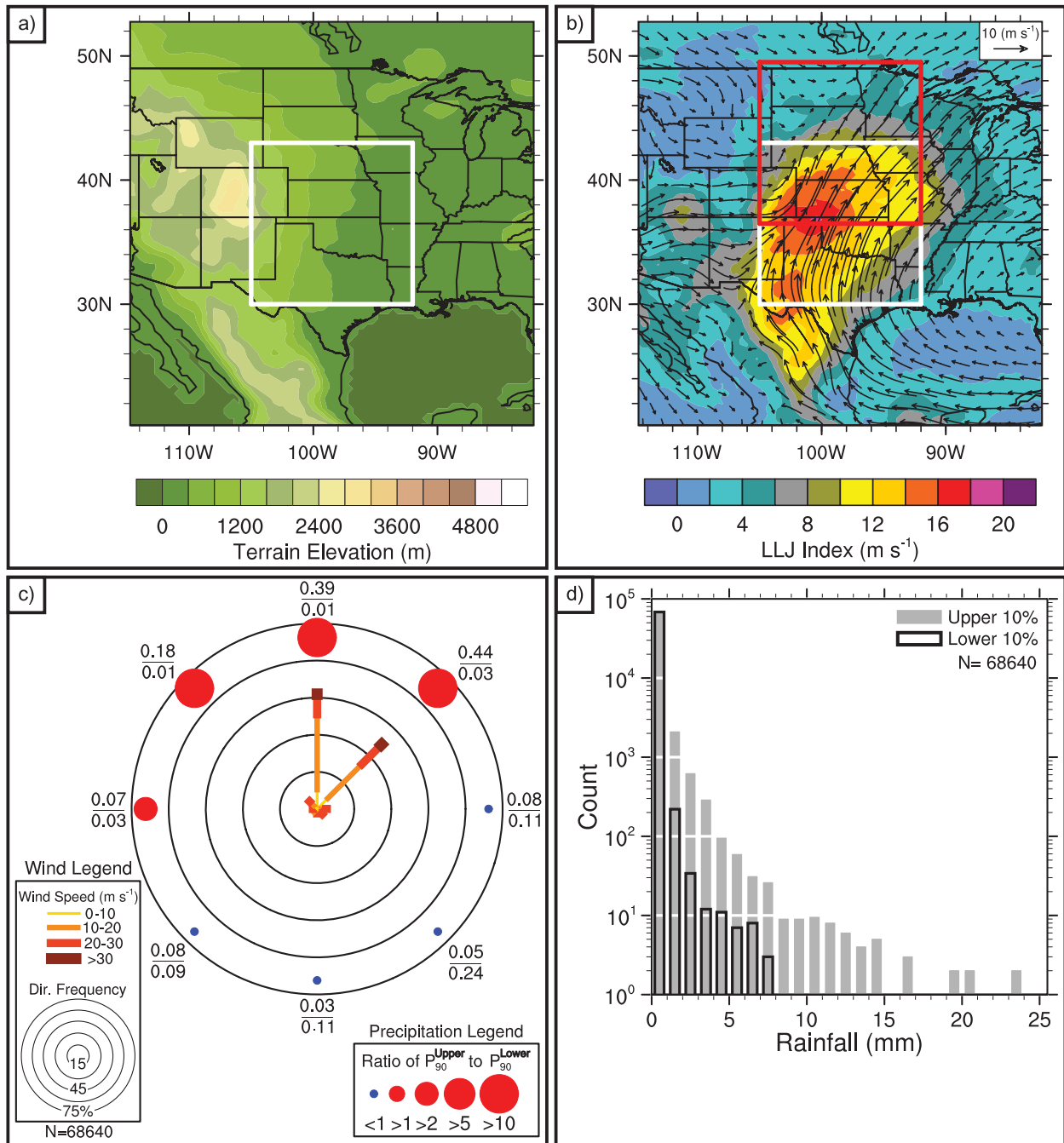
FIG. 6. Composite of LLJ events and the associated precipitation statistics for the GPLLJ (region 1; Fig. 1 and Table 1) for July. Shown are the (a) terrain elevation (m MSL) within the region; (b) the mean NLLJ index (m s^{-1}) and 500-m-AGL winds (arrows) for the upper 10th percentile of events defined within the white box for 1985–2005; (c) the distributions of wind direction and wind speed for the upper 10th percentile of NLLJ events, where distributions are constructed from values at all grid points within the white box; and (d) the distributions of nocturnal precipitation (mm h^{-1}) for strong events (≥90th percentile; gray) and weak events (≤10th percentile; black outlines) within the dominant exit region of the NLLJ [red box in (b)]. The wind direction distributions in (c) are plotted such that the winds blowing to the north point northward (opposite of the convention), to highlight the relationship between the moisture transport, baroclinity, and lift within the exit region to the accompanying precipitation. The ratio of the 90th percentile of nocturnal precipitation for the strongest (P_{90}^{Upper}) and the weakest (P_{90}^{Lower}) NLLJ events within each of the eight rainfall boxes are plotted on the perimeter of the wind rose in (c).
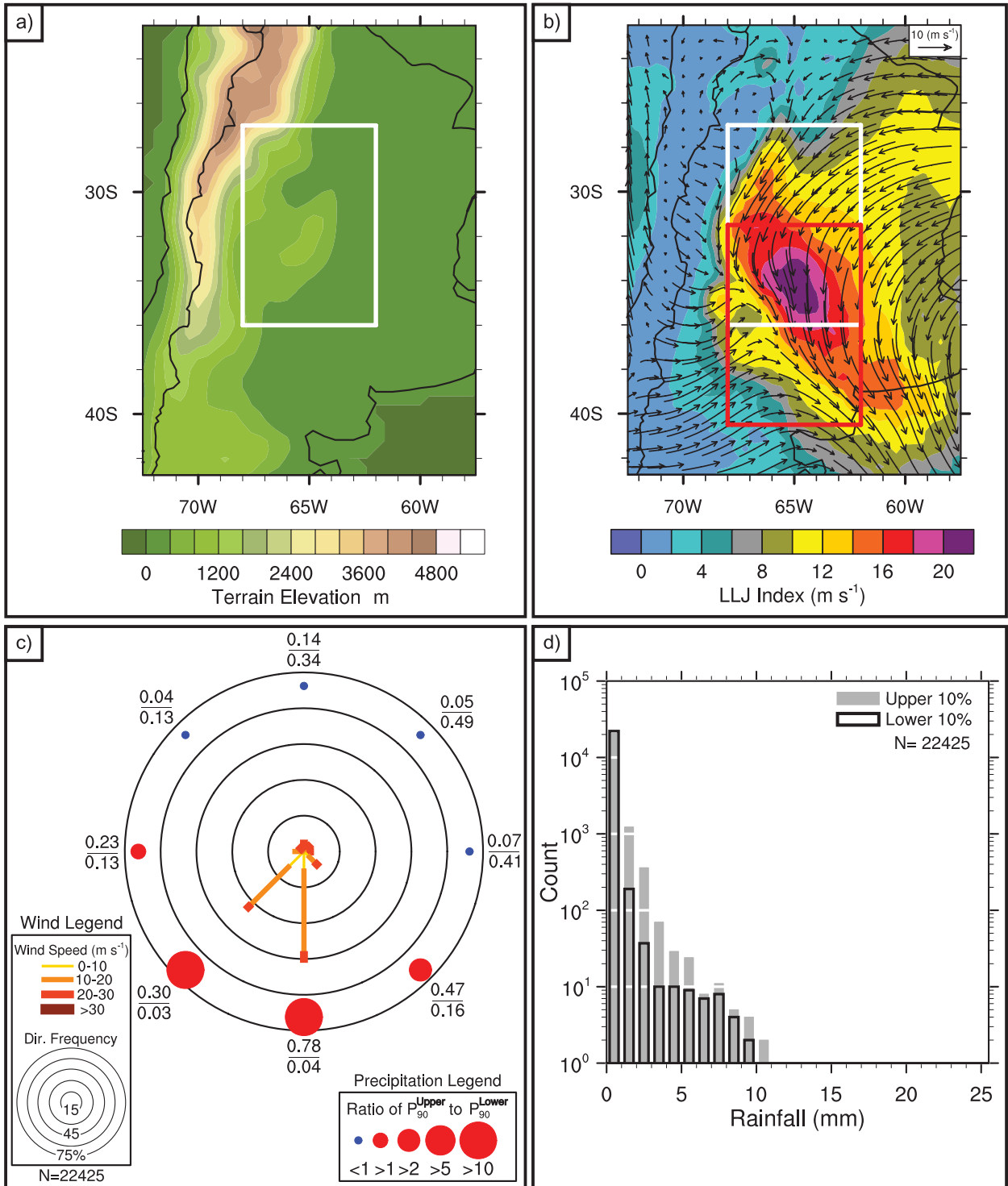
FIG. 7. As in Fig. 6, but for the component of the SALLJ that is most prevalent in Argentina (region 13; Fig. 1 and Table 1) in January.

Fig. 6b). The winds associated with the China NLLJ are often strong, occasionally exceeding 30 m s^{-1} (Fig. 9c). However, the NLLJ index is relatively weak (Fig. 9b) compared to the GPLLJ (Fig. 6b). Because the NLLJ index is designed to minimize the influence of synoptic activity and emphasize the influence of diurnal forcing, it is possible that large-scale forcing plays a more important role in modulating the China NLLJ than it does for the
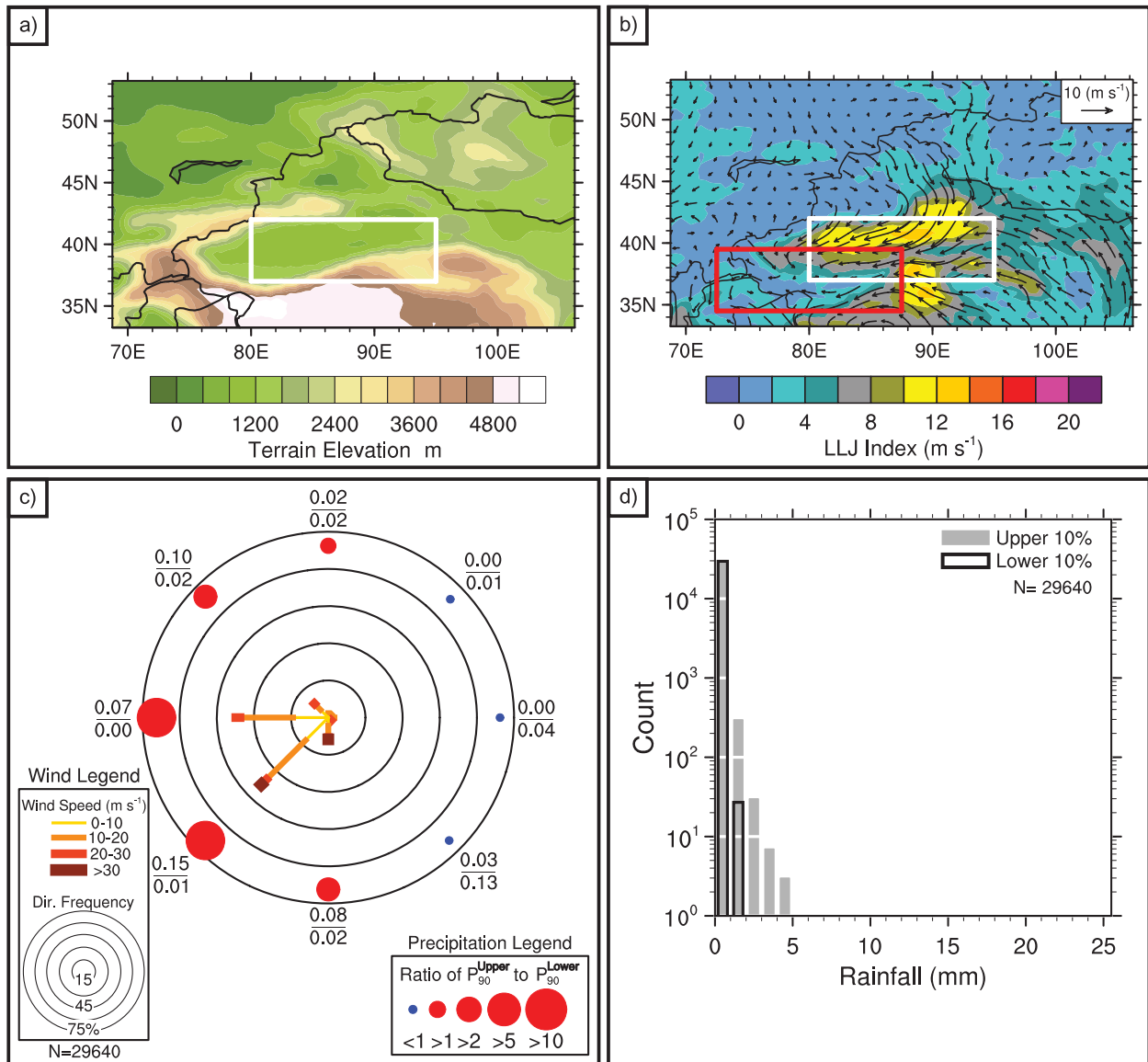
FIG. 8. As in Fig. 6, but for the Tarim Pendi region (region 7; Fig. 1 and Table 1) in July.

GPLLJ. Nocturnal rainfall extremes are enhanced in the exit region during strong China NLLJ events (Fig. 9c), and the rainfall distributions for the strongest and weakest NLLJ events are statistically distinct in the north and northwest rainfall boxes (Table 1). In the north region, higher-intensity rainfall (>1 mm h^{-1}) is commonly 2–3 times greater for the strongest NLLJ events compared to the weakest events. Interestingly, despite frequent strong NLLJ events in the northeast rainfall box (Fig. 9c), the rainfall distributions for the strongest and weakest NLLJ events are not statistically distinct (Table 1). Inspection of Fig. 9c indicates that even though P_{90}^{Upper} in the northeast rainfall box (the numerator) is about the same magnitude as for the north and northwest rainfall boxes,

P_{90}^{Lower} (the denominator) is substantially larger than for the north and northwest rainfall boxes. A recent study (Yin et al. 2009) indicates that precipitation in eastern China undergoes a smaller diurnal cycle compared to that farther westward (corresponding to the north and northwest rainfall boxes), which is also evident in Fig. 3d. Therefore, it is possible that thunderstorm activity in eastern China initiated during the late afternoon due to boundary layer instability lasts into the nighttime and dampens the signal of rainfall variability that may be associated with the China NLLJ in the northeast rainfall box.

The results for the NLLJ in Namibia–Angola during austral summer are shown in Fig. 10. The jet is partly
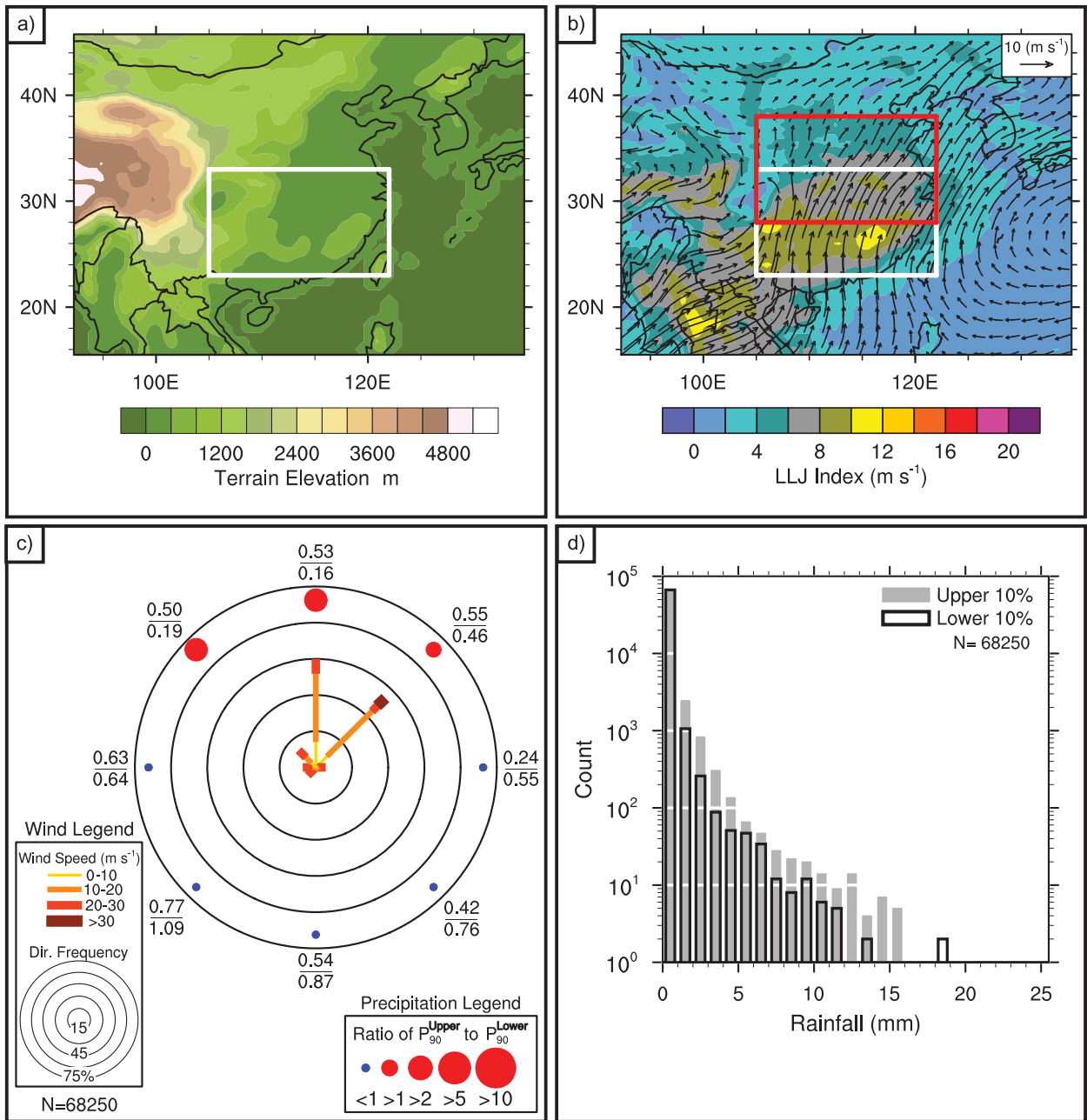
FIG. 9. As in Fig. 6, but for southeast China (region 10; Fig. 1 and Table 1) in July.

driven by the sharp land–sea temperature contrast that develops during the day and is accentuated by heating over the elevated terrain of the Kalahari Desert farther inland (R10; Lindesay and Tyson 1990). A comparatively unique feature associated with the NLLJ is the low pressure circulation centered along the eastern edge of the core box in Angola (Fig. 10b). The location of the low pressure on the downwind side of the mountain escarpment (Fig. 10a) suggests that its formation is related to lee-side effects from NLLJ-enhanced flow around

and over the mountains, similar to lee cyclones that form elsewhere (e.g., Chung 1977; Aebischer and Schär 1998). The rainfall distributions for the strongest and weakest NLLJ events are statistically distinct in the northeast, east, southeast, south, and southwest rainfall boxes (Fig. 10c and Table 1). In the east rainfall box (the primary exit region), higher-intensity rainfall (>1 mm h^{-1}) is commonly one to two orders of magnitude greater for the strongest NLLJ events compared to the weakest events (Fig. 10d). Interestingly, the comparatively large ratios
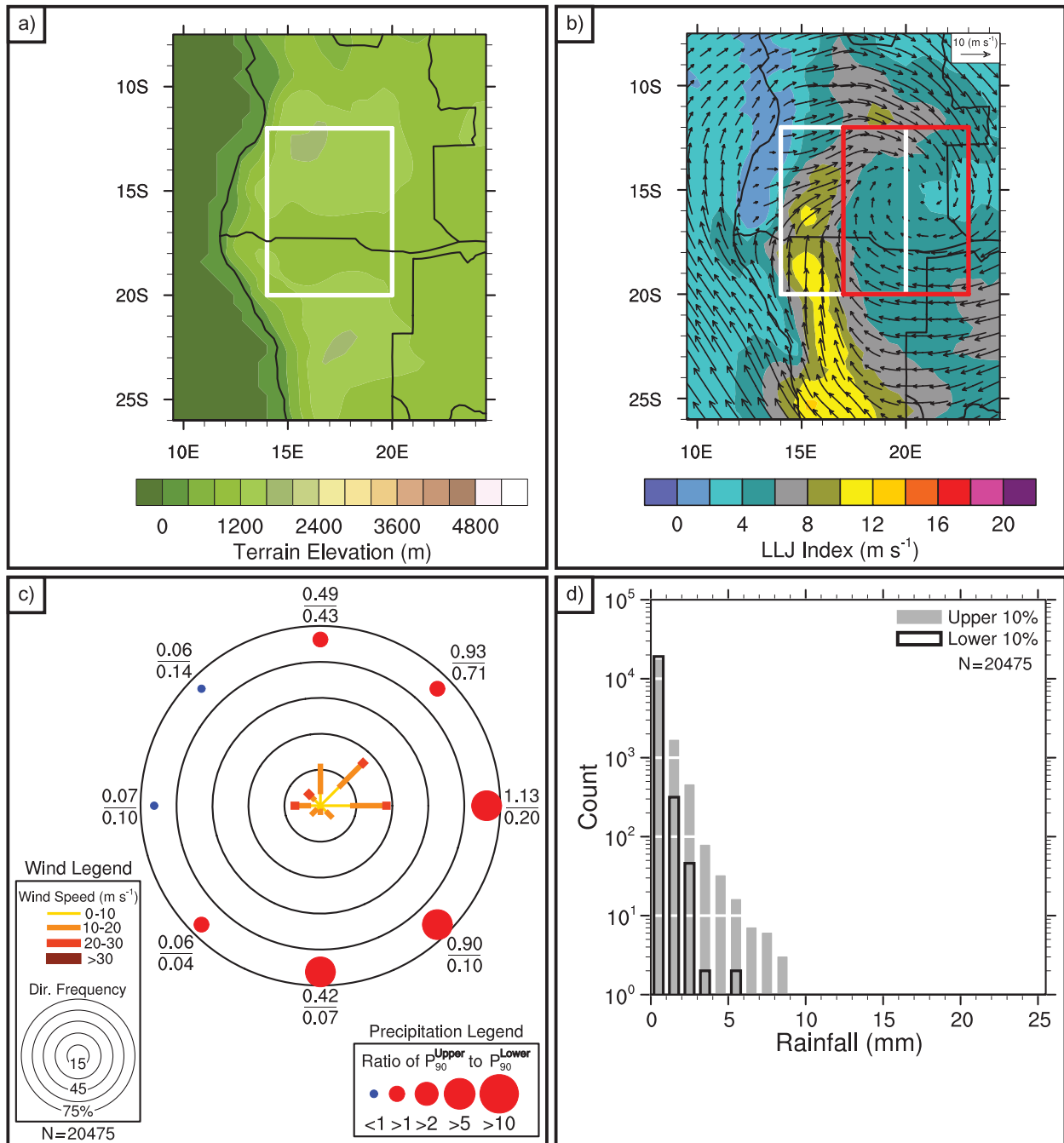
FIG. 10. As in Fig. 6, but for Namibia–Angola (region 15; Fig. 1 and Table 1) in January.

($P_{90}^{\text{Upper}}/P_{90}^{\text{Lower}}$) in the southeast, south, and southwest rainfall boxes do not appear to be associated with the NLLJ terminus (Fig. 10c). Rather, the unique low pressure center mentioned earlier has easterly and southeasterly winds on its southern side (Fig. 10b) that flow into these southern rainfall boxes. The circulation enhances upslope flow on the east and southeast sides of the mountain escarpments in Namibia and Angola and

leads to orographic precipitation in the southern tier of rainfall boxes. To our knowledge, this is the first time the relationship of the Namibia–Angola NLLJ with nocturnal rainfall extremes has been documented.

The results for the NLLJ in Syria during boreal summer are shown in Fig. 11. The Syria NLLJ was chosen because it is not previously documented and because it represents an example for which an NLLJ does not
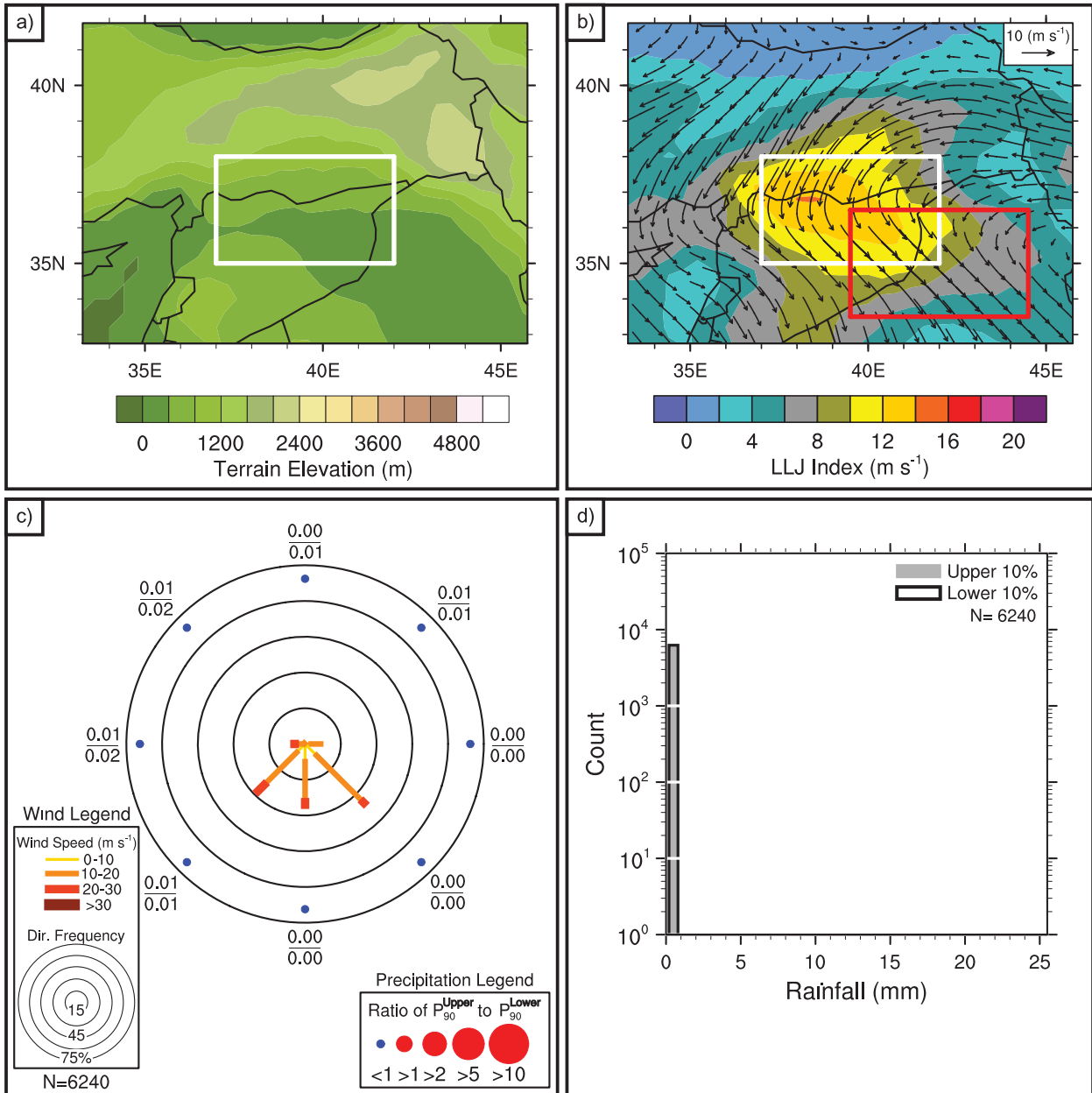
FIG. 11. As in Fig. 6, but for Syria (region 4; Fig. 1 and Table 1) in July.

have a discernable impact on nocturnal rainfall extremes (Figs. 11c,d and Table 1). The NLLJ core is surrounded by the Taurus Mountains of Turkey to the north, the Mediterranean coast immediately to the west, and the Euphrates River Valley in the southeast (Fig. 11a). The diurnally varying mountain-valley breeze over the Taurus Mountains may play a role in the onset and maintenance of the jet. Also, downslope drainage from the mountains into the NLLJ exit region within the Euphrates River Valley (Fig. 11b) would almost certainly

have a drying effect, leaving very little moisture to form precipitation.

The six NLLJs discussed above provide a representative sample of the eighteen regions analyzed in this study (Table 1). There are numerous statistically significant linkages between NLLJ exit regions and nocturnal rainfall, including the Great Plains, Tibet, Tarim Pendi, India, Southeast Asia, and southeast China in boreal summer and Argentina, Namibia–Angola, Botswana, and Ethiopia in austral summer. NLLJs that are weakly or indeterminately

TABLE 2. Percentage of extreme nocturnal rainfall events occurring in the primary NLLJ exit box for the top 25th and top 10th percentiles of NLLJ events during the most active month in each region (Table 1). Rainfall extremes are defined as events that exceed the 90th percentile of the 21-yr daily 0000–0400 UTC mean rainfall totaled for all grid points in the exit region box.

No.	Region	Percent of extreme rainfall events occurring during top 25% of NLLJ events	Percent of extreme rainfall events occurring during top 10% of NLLJ events
1	GPLLJ	46	25
2	North Venezuela	40	20
3	Maracaibo	23	11
4	Syria*	—	—
5	Iran	15	2
6	Tibet	38	15
7	Tarim Pendi	51	23
8	India	28	15
9	Southeast Asia	42	22
10	China	40	14
11	Venezuela	12	5
12	Guyana	18	9
13	Argentina	42	14
14	Brazil	20	3
15	Namibia	48	20
16	Botswana	45	25
17	Ethiopia	31	18
18	Australia	15	6

* There are no data for Syria because no nocturnal rainfall occurs in the primary NLLJ box.

associated with nocturnal rainfall include northern Venezuela, Maracaibo, Syria, and Iran in boreal summer and Venezuela, Guyana, Brazil, and Australia in austral summer. We have assumed that all NLLJs peak at or near local midnight and that rainfall extremes associated with the NLLJs occur between 0000 and 0400 LST. Thus, some NLLJ regions with indeterminate relationships to rainfall (e.g., northern Venezuela, Brazil) may have stronger connections to nocturnal rainfall either earlier or later than our assumed midnight peak. Despite this limitation, the existing approach clearly establishes widespread linkages between NLLJs and nocturnal rainfall extremes.

5. Conclusions

R10 introduced the 21-yr, hourly, global 40-km CFDDA reanalysis and demonstrated that it realistically simulates the vertical, horizontal, and diurnal structure of the winds in well-known NLLJ regions. The global distribution of NLLJs during January and July was examined by employing a new index of NLLJ activity based on the vertical structure of the wind's temporal variation, a methodology made possible by the availability of hourly three-dimensional output from CFDDA. The index resolved all the known NLLJs (Stensrud 1996) and a number of newly identified jets. Several NLLJs were analyzed to understand the mechanisms that give rise to them.

In this paper, we investigated the linkages of nocturnal rainfall extremes with the NLLJs identified by R10. It was demonstrated that CFDDA reasonably replicates the diurnal cycle, extremes, and spatial structure of globally rainfall compared to satellite-based precipitation datasets. A statistical approach was introduced to categorize nocturnal precipitation extremes as a function of the NLLJ magnitude and wind direction/frequency in a consistent manner globally. For two well-known NLLJs (the U.S. Great Plains and northern Argentina), our results agree with previous studies, which established a strong relationship between the occurrence of NLLJs and nocturnal rainfall extremes. This demonstrates the veracity of our methodology. Significant seasonal linkages between NLLJs and nocturnal precipitation extremes exist in at least 10 disparate regions around the world, including the U.S. Great Plains, Tibet, Tarim Pendi (northwest China), India, Southeast Asia, southeast China, Argentina, Namibia–Angola, Botswana, and Ethiopia. In many regions, the nocturnal precipitation extremes associated with strong NLLJs account for a disproportionate fraction of all nocturnal extreme events (Table 2). For example, the top 25% of NLLJ events account for more than 40% of the extreme rainfall events within the U.S. Great Plains, Tarim Pendi, Southeast Asia, China, Argentina, Namibia–Angola, and Botswana. It is clear from Table 2 that NLLJs play an important role in the climatology of extreme precipitation; in several cases NLLJ exit regions coincide with heavily populated metropolitan areas (e.g., China, Southeast Asia).

For many jets, we have shown a physical linkage exists between the jet exit region and enhanced precipitation. Previous studies have shown that mesoscale ascending motion often occurs near the terminus of the NLLJ either because of the jet encountering an upward terrain slope or a frontal zone. However, for other jets, such as those found in Guyana, Venezuela, Australia, India, and Brazil, the relationship to the jet exit region is unclear. Interestingly, all these regions have a significant coastal influence. In many coastal regions, the diurnal cycle within the coastal zone tends to produce convection onshore during the daytime and offshore at night. NLLJs in coastal regions are often oriented parallel to the coast at latitudes where Coriolis effects are important, whereas NLLJs near the equator are oriented in the onshore direction. Collectively, these factors can cause the relationship between nocturnal precipitation and the jet exit region to be unclear. However, it is noteworthy that the Indian jet is associated with enhanced precipitation in nearly all rainfall boxes (Table 1). This suggests that the jet is important in transporting moisture into the general region, rather than just the exit region. Indeed, this jet is partly a manifestation of the Indian monsoon. An intriguing possibility is that the formation of NLLJs augments the moisture transport within the monsoon system. A future analysis of the source regions, transport, and convergence of moisture as related to NLLJs would likely shed additional light on how NLLJs enhance or suppress precipitation.

The amplitude of the daily cycle of near-surface temperature is changing across the globe, in part because of anthropogenic greenhouse gas increases linked to global warming (Zhou et al. 2010). Thus, any alteration to the diurnal cycle in a given region may affect the positioning, magnitude, and frequency of NLLJs and ultimately the regional hydrologic cycle. If so, possible impacts include changes in the frequency of severe flooding in heavily populated NLLJ regions such as China and India or modified hydrologic cycles in important agricultural regions such as the U.S. Great Plains and Southeast Asia. There is a clear need for future investigations of how rainfall extremes are impacted by shifts in NLLJs and how NLLJs may be changing (or might change in the future) as a result of regional climate trends.

REFERENCES

Adler, R. F., and Coauthors, 2003: The Version 2 Global Precipitation Climatology Project (GPCP) Monthly Precipitation Analysis (1979–present). *J. Hydrometeor.,* **4,** 1147–1167.

Aebischer, U., and C. Schär, 1998: Low-level potential vorticity and cyclogenesis to the lee of the Alps. *J. Atmos. Sci.,* **55,** 186–207.

Arritt, R. W., T. D. Rink, M. Segal, D. P. Todey, C. A. Clark, M. J. Mitchell, and K. M. Labas, 1997: The Great Plains low-level jet during the warm season of 1993. *Mon. Wea. Rev.,* **125,** 2176–2192.

Augustine, J. A., and K. W. Howard, 1991: Mesoscale convective complexes over the United States during 1986 and 1987. *Mon. Wea. Rev.,* **119,** 1575–1589.

——, and F. Caracena, 1994: Lower-tropospheric precursors to nocturnal MCS development over the central United States. *Wea. Forecasting,* **9,** 116–135.

Bonner, W. D., 1968: Climatology of the low level jet. *Mon. Wea. Rev.,* **96,** 833–850.

Byerle, L. A., and J. Paegle, 2003: Modulation of the Great Plains low-level jet and moisture transports by orography and large-scale circulations. *J. Geophys. Res.,* **108,** 8611, doi:10.1029/2002JD003005.

Carbone, R. E., and J. D. Tuttle, 2008: Rainfall occurrence in the U.S. warm season: The diurnal cycle. *J. Climate,* **21,** 4132–4146.

Chen, G. T.-J., and C. C. Yu, 1988: Study of low-level jet and extremely heavy rainfall over northern Taiwan in the mei-yu season. *Mon. Wea. Rev.,* **116,** 884–891.

Chung, Y.-S., 1977: On the orographic influence and lee cyclogenesis in the Andes, the Rockies, and the East Asian Mountains. *Meteor. Atmos. Phys.,* **26,** 1–12.

Dai, A., 2001: Global precipitation and thunderstorm frequencies. Part II: Diurnal variations. *J. Climate,* **14,** 1112–1128.

——, and K. E. Trenberth, 2004: The diurnal cycle and its depiction in the Community Climate System Model. *J. Climate,* **17,** 930–951.

Ebert, E. E., J. E. Janowiak, and C. Kidd, 2007: Comparison of near-real-time precipitation estimates from satellite observations and numerical models. *Bull. Amer. Meteor. Soc.,* **88,** 47–64.

Findlater, J., 1969: A major low-level air current near the Indian Ocean during the northern summer. *Quart. J. Roy. Meteor. Soc.,* **95,** 362–380.

Helfand, H. M., and S. D. Schubert, 1995: Climatology of the simulated Great Plains low-level jet and its contribution to the continental moisture budget of the United States. *J. Climate,* **8,** 784–806.

Hering, W. S., and T. R. Borden, 1962: Diurnal variations in the summer wind field over the central United States. *J. Atmos. Sci.,* **19,** 81–86.

Higgins, R. W., Y. Yao, E. S. Yarosh, J. E. Janowiak, and K. C. Mo, 1997: Influence of the Great Plains low-level jet on summertime precipitation and moisture transport over the central United States. *J. Climate,* **10,** 481–507.

Janowiak, J. E., V. E. Kousky, and R. J. Joyce, 2005: Diurnal cycle of precipitation determined from the CMORPH high spatial and temporal resolution global precipitation analyses. *J. Geophys. Res.,* **110,** D23105, doi:10.1029/2005JD006156.

Jones, P. W., 1999: First- and second-order conservative remapping schemes for grids in spherical coordinates. *Mon. Wea. Rev.,* **127,** 2204–2210.

Joseph, P. V., and S. Sijikumar, 2004: Intraseasonal variability of the low-level jet stream of the Asian summer monsoon. *J. Climate,* **17,** 1449–1458.

Joyce, R. J., J. E. Janowiak, P. A. Arkin, and P. Xie, 2004: CMORPH: A method that produces global precipitation estimates from passive microwave and infrared data at high spatial and temporal resolution. *J. Hydrometeor.,* **5,** 487–503.

Knievel, J. C., D. A. Ahijevych, and K. W. Manning, 2004: Using temporal modes of rainfall to evaluate the performance of a numerical weather prediction model. *Mon. Wea. Rev.,* **132,** 2995–3009.

Lee, M.-I., and Coauthors, 2007: An analysis of the warm-season diurnal cycle over the continental United States and northern Mexico in general circulation models. *J. Hydrometeor.,* **8,** 344–366.

Lin, Y., and K. E. Mitchell, 2005: The NCEP stage II/IV hourly precipitation analyses: Development and applications. Preprints, *19th Conf. on Hydrology,* San Diego, CA, Amer. Meteor. Soc., 1.2. [Available online at http://ams.confex.com/ams/pdfpapers/83847.pdf.]

Lindesay, J. A., and P. D. Tyson, 1990: Thermo-topographically induced boundary layer oscillations over the central Namib, southern Africa. *Int. J. Climatol.,* **10,** 1990.

Mann, H. B., and D. R. Whitney, 1947: On a test of whether one of two random variables is stochastically larger than the other. *Ann. Math. Stat.,* **18,** 50–60.

Marengo, J. A., W. R. Soares, C. Saulo, and M. Nicolini, 2004: Climatology of the low-level jet east of the Andes as derived from the NCEP–NCAR reanalyses: Characteristics and temporal variability. *J. Climate,* **17,** 2261–2280.

Means, L. L., 1952: On thunderstorm forecasting in the central United States. *Mon. Wea. Rev.,* **80,** 165–189.

Miller, D., and J. M. Fritsch, 1991: Mesoscale convective complexes in the western Pacific region. *Mon. Wea. Rev.,* **119,** 2978–2992.

Mitchell, M. J., R. W. Arritt, and K. Labas, 1995: A climatology of the warm season Great Plains low-level jet using wind profiler observations. *Wea. Forecasting,* **10,** 576–591.

Mo, K. C., and E. H. Berbery, 2004: Low-level jets and the summer precipitation regimes over North America. *J. Geophys. Res.,* **109,** D06117, doi:10.1029/2003JD004106.

Nicolini, M., and A. C. Saulo, 2006: Modeled Chaco low-level jets and related precipitation patterns during the 1997–1998 warm season. *Meteor. Atmos. Phys.,* **94,** 129–143.

Nogués-Paegle, J., and K. C. Mo, 1997: Alternating wet and dry conditions over South America during summer. *Mon. Wea. Rev.,* **125,** 279–291.

Pitchford, K. L., and J. London, 1962: The low-level jet as related to nocturnal thunderstorms over midwest United States. *J. Appl. Meteor.,* **1,** 43–47.

Pryor, S. C., J. A. Howe, and K. E. Kunkel, 2009: How spatially coherent and statistically robust are temporal changes in extreme precipitation in the contiguous USA? *Int. J. Climatol.,* **29,** 31–45.

Rife, D. L., J. O. Pinto, A. J. Monaghan, C. A. Davis, and J. R. Hannon, 2010: Global distribution and characteristics of diurnally varying low-level jets. *J. Climate,* **23,** 5041–5064.

Rodgers, J. L., and W. A. Nicewander, 1988: Thirteen ways to look at the correlation coefficient. *Amer. Stat.,* **42,** 59–66.

Salio, P., M. Nicolini, and A. C. Saulo, 2002: Chaco low-level jet events characterization during the austral summer season. *J. Geophys. Res.,* **107,** 4816, doi:10.1029/2001JD001315.

——, ——, and E. J. Zipser, 2007: Mesoscale convective systems over southeastern South America and their relationship with the South American low-level jet. *Mon. Wea. Rev.,* **135,** 1290–1309.

Solomon, S., D. Qin, M. Manning, M. Marquis, K. Averyt, M. M. B. Tignor, H. L. Miller Jr., and Z. Chen, Eds., 2007: *Climate Change 2007: The Physical Science Basis.* Cambridge University Press, 996 pp.

Song, J., K. Liao, R. L. Coulter, and B. M. Lesht, 2005: Climatology of the low-level jet at the southern Great Plains atmospheric boundary layer experiments site. *J. Appl. Meteor.,* **44,** 1593–1606.

Stensrud, D. J., 1996: Importance of low-level jets to climate: A review. *J. Climate,* **9,** 1698–1711.

Trier, S. B., C. A. Davis, D. A. Ahijevych, M. L. Weisman, and G. H. Bryan, 2006: Mechanisms supporting long-lived episodes of propagating nocturnal convection within a 7-day WRF model simulation. *J. Atmos. Sci.,* **63,** 2437–2461.

Tuttle, J. D., and C. A. Davis, 2006: Corridors of warm season precipitation in the central United States. *Mon. Wea. Rev.,* **134,** 2297–2317.

Vera, C., and Coauthors, 2006: The South American Low-Level Jet Experiment. *Bull. Amer. Meteor. Soc.,* **87,** 63–77.

Vernekar, A. D., B. P. Kirtman, and M. J. Fennessy, 2003: Low-level jets and their effects on the South American summer climate as simulated by the NCEP Eta model. *J. Climate,* **16,** 297–311.

Wallace, J., 1975: Diurnal variations in precipitation and thunderstorm frequency over the conterminous United States. *Mon. Wea. Rev.,* **103,** 406–419.

Weaver, S. J., and S. Nigam, 2008: Variability of the Great Plains low-level jet: Large-scale circulation context and hydroclimate impacts. *J. Climate,* **21,** 1532–1551.

Whiteman, C. D., X. Bian, and S. Zhong, 1997: Low-level jet climatology from enhanced rawinsonde observations at a site in the southern Great Plains. *J. Appl. Meteor.,* **36,** 1363–1376.

Wilks, D. S., 2006: *Statistical Methods in the Atmospheric Sciences.* 2nd ed. International Geophysical Series, Vol. 91, Academic Press, 627 pp.

Yin, S., D. Chen, and Y. Xie, 2009: Diurnal variations of precipitation during the warm season over China. *Int. J. Climatol.,* **29,** 1154–1170.

Zhang, C., P. Woodworth, and G. Guojun, 2006: The seasonal cycle in the lower troposphere over West Africa from sounding observations. *Quart. J. Roy. Meteor. Soc.,* **132,** 2559–2582.

Zhou, L., R. E. Dickinson, A. Dai, and P. Dirmeyer, 2010: Detection and attribution of anthropogenic forcing to diurnal temperature range changes from 1950-1999: Comparing multi-model simulations with observations. *Climate Dyn.,* doi:10.1007/s00382-009-0644-2, in press.

Zunckel, M., G. Held, R. A. Preston-Whyte, and A. Joubert, 1996: Low-level wind maxima and the transport of pyrogenic products over southern Africa. *J. Geophys. Res.,* **101,** 23 745–23 755.